

All-in-One Heptamethine Cyanine Amphiphiles for Dual Imaging-Guided Chemo-Photodynamic-Photothermal Therapy of Breast Cancer

Yu Li, Jing Zhang, Lijun Zhu, Mou Jiang, Changsheng Ke, Hanxiong Long, Ruoyun Lin, Chaohui Ye, Xin Zhou, Zhong-Xing Jiang,* and Shizhen Chen*

Developing a theranostic system that integrates multimodal imaging, synergistic therapeutic, and formulation entities is a promising strategy for efficient cancer treatment. However, the complexity and safety concerns of multiple functional entities hinder their clinical translation. Herein, versatile “all-in-one” heptamethine cyanine amphiphiles (PEG-Cy-Fs) with multiple favorable capabilities, including fluorine-19 magnetic resonance imaging (^{19}F MRI), near-infrared fluorescence imaging (NIR FLI), photodynamic therapy (PDT), photothermal therapy (PTT), polyethylene glycolation (PEGylation) and high biocompatibility, are developed for the convenient construction of theranostic platforms. Amphiphiles PEG-Cy-Fs are synthesized on a multi-hundred-milligram scale with high efficacy, which self-assembled with a chemotherapy drug tamoxifen (TAM) into monodisperse and stable nanoparticles (SoFoTm/PEG-Cy-F₁₈) with “turned on” FLI, sensitive ^{19}F MRI, mitochondria-targeting ability, high PDT and PTT efficacy, and PEGylation-optimized pharmacokinetics. The selective accumulation of SoFoTm/PEG-Cy-F₁₈ in xenograft MCF-7 tumor with a long retention time (>10 days) enabled ^{19}F MRI-NIR FLI-guided chemo-photodynamic-photothermal therapy (chemo-PDT-PTT) of breast cancer with high therapeutical index in mice. The “all-in-one” heptamethine cyanine amphiphile may facilitate the convenient and standardized preparation of high-performance theranostics systems for clinical translation.

1. Introduction

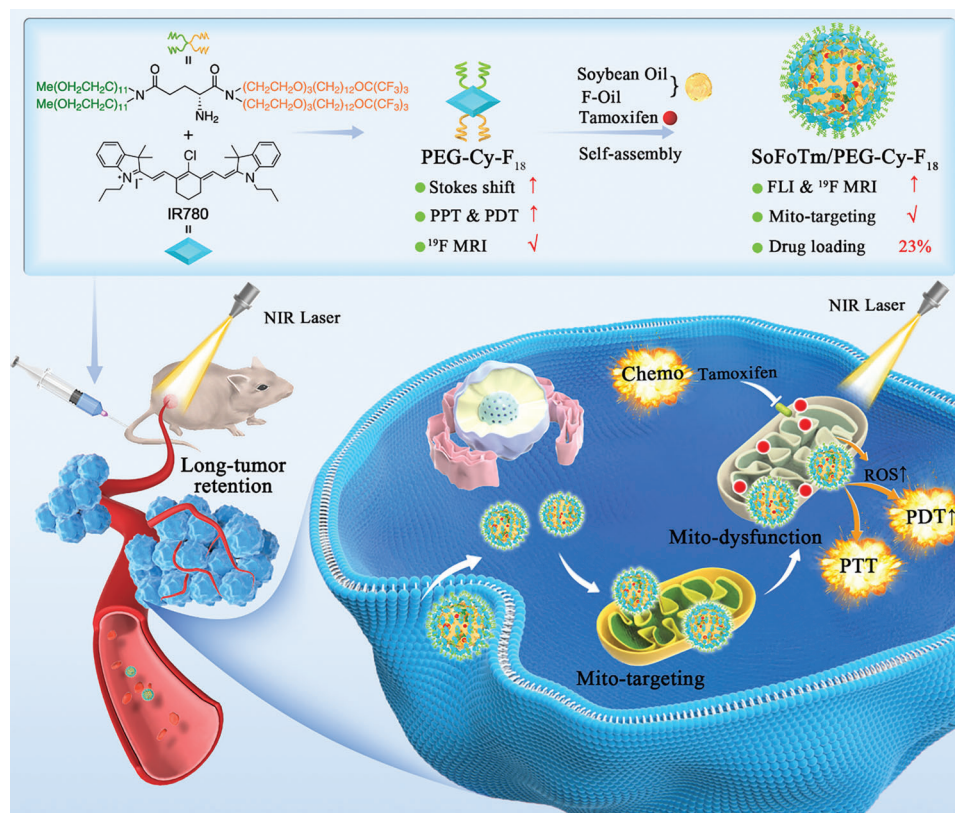
The complexity and heterogeneity of tumors seriously undermine the efficacy of conventional cancer therapy, which propelled the development of multifunctional theranostics for multimodal imaging-guided synergistic cancer therapy.^[1] Combination therapy has the potential to increase antitumor efficacy and reduce drug resistance compared to monotherapy.^[2] In cancer therapy, phototherapy, which includes photodynamic therapy (PDT) and photothermal therapy (PTT), has become a well-established combination partner for chemotherapy due to its spatiotemporal selectivity and limited multi-drug resistance.^[3] On the imaging side, multimodal imaging provides comprehensive “drug-tumor-therapy” information, such as drug targeting efficacy, pharmacokinetics, tumor microenvironment, therapeutic responses, etc., allowing for accurate and efficient personalized cancer treatment.^[4] Among various imaging modalities, the combination of near-infrared fluorescence imaging (NIR FLI) and fluorine-19 magnetic resonance imaging (^{19}F MRI) is highly valuable.^[5] NIR FLI can conveniently provide real-time images with high

Y. Li, M. Jiang, C. Ye, X. Zhou, Z.-X. Jiang, S. Chen
State Key Laboratory of Magnetic Resonance and Atomic and Molecular Physics
National Center for Magnetic Resonance in Wuhan
Wuhan Institute of Physics and Mathematics
Innovation Academy for Precision Measurement Science and Technology
Chinese Academy of Sciences-Wuhan National Laboratory for Optoelectronics
Wuhan 430071, China
E-mail: zxjiang@whu.edu.cn; chenshizhen@wipm.ac.cn

Y. Li, M. Jiang, C. Ye, X. Zhou, Z.-X. Jiang, S. Chen
University of Chinese Academy of Sciences
Beijing 100049, China
J. Zhang
School of Life Science and Engineering
Lanzhou University of Technology
Lanzhou 730050, China
L. Zhu, C. Ke, H. Long, R. Lin
School of Pharmaceutical Sciences
Wuhan University
Wuhan 430071, China
C. Ye, X. Zhou, S. Chen
Optics Valley Laboratory
Hubei 430074, China
Z.-X. Jiang
Key Laboratory of Organofluorine Chemistry
Shanghai Institute of Organic Chemistry
Chinese Academy of Sciences
Shanghai 200032, China

 The ORCID identification number(s) for the author(s) of this article can be found under <https://doi.org/10.1002/adhm.202300941>

DOI: 10.1002/adhm.202300941



Scheme 1. Schematic illustration of versatile theranostic SoFoTm/PEG-Cy-F₁₈ nanoparticles, which were self-assembled from PEG-Cy-F₁₈, soybean oil, F-oil, and TAM for NIR FLI-¹⁹F MRI dual-modal imaging-guided chemo-PTT-PDT of breast cancer.

sensitivity and relatively deep detection depth, but it still has difficulty in monitoring deep organs. ¹⁹F MRI complements FLI by providing quantitative high-contrast “hot spot” images without tissue depth limits and background signals, and it is free of ionizing radiation. Therefore, integrating phototherapy, chemotherapy, NIR FLI, and ¹⁹F MRI into one theranostic system holds great potential to improve the precision and effectiveness of cancer treatment.

Despite all the merits mentioned above, constructing such a theranostic platform usually demands complex ingredients and tedious preparation processes. Typically, theranostics integrate both imaging agents (e.g., fluorescence dyes and MRI contrast agents) and therapeutic agents (e.g., chemotherapy drugs and photosensitizers) into a nanocarrier (e.g., polymers, Au nanoparticles, graphenes, and quantum dots), which are subsequently coated with hydrophilic polymers (e.g., polyethylene glycols (PEGs), hyaluronic acid) to increase water solubility, improve biocompatibility and prolong blood circulation time.^[6] However, the complexity of functional integration and safety concerns associated with multiple ingredients can severely hinder the clinical translation of multifunctional theranostics.^[7] To address these limitations, “all-in-one” self-assembled amphiphiles that could simultaneously act as a multimodal imaging agent, photosensitizer, and nanocarrier are highly desired.^[8]

In this study, PEGylated and fluorinated heptamethine amphiphiles denoted as PEG-Cy-Fs with FLI, ¹⁹F MRI, PDT, and PTT theranostic functions were synthesized and applied to

engineering NIR light-responsive nanosystems for ¹⁹F MR-FLI dual imaging-guided chemo-PDT-PTT of cancer in a precise and tunable way (Scheme 1). The core of PEG-Cy-Fs is IR780, the first NIR heptamethine cyanine dye with photodynamic and photothermal capabilities under the same wavelength of 808 nm, and exhibits mitochondria-targeting ability in multiple cancer cells.^[9] To construct PEG-Cy-Fs, we utilized fluorinated amphiphilic building blocks to replace the chlorine atom on the polyene of IR780, which not only addresses the poor water solubility of IR780 but also endows it with ¹⁹F MRI and self-assembly capabilities. Notably, we employed linear and branched monodisperse PEG, respectively, to optimize the physicochemical and imaging properties of PEG-Cy-Fs. Owing to its higher ¹⁹F MRI sensitivity and aggregation tendency, PEG-Cy-F₁₈, with branched monodisperse PEG and fluorinated alkyl chains, was then employed to load tamoxifen (TAM), a clinical breast cancer drug that can target mitochondria, to achieve synergistic chemo-photothermal-photodynamic therapy for breast cancer.^[10] Additionally, soybean oil, a hydrophobic oil widely used in pharmaceutical formulation,^[11] was employed to reduce PEG-Cy-F₁₈ self-quenching in water and thus “turns on” the fluorescence (FL). To improve the ¹⁹F MRI sensitivity, we employed 1,11-diperfluoro-*tert*-butoxyundecane (F-oil), which gave an overlapped ¹⁹F signal to PEG-Cy-F₁₈, to partially replace the soybean oil and thus improve the ¹⁹F MRI signal intensity without introducing chemical shift artifacts.^[12] Notably, fluorocarbons are well-known for their high oxygen solubility,^[13] which may deliver oxygen

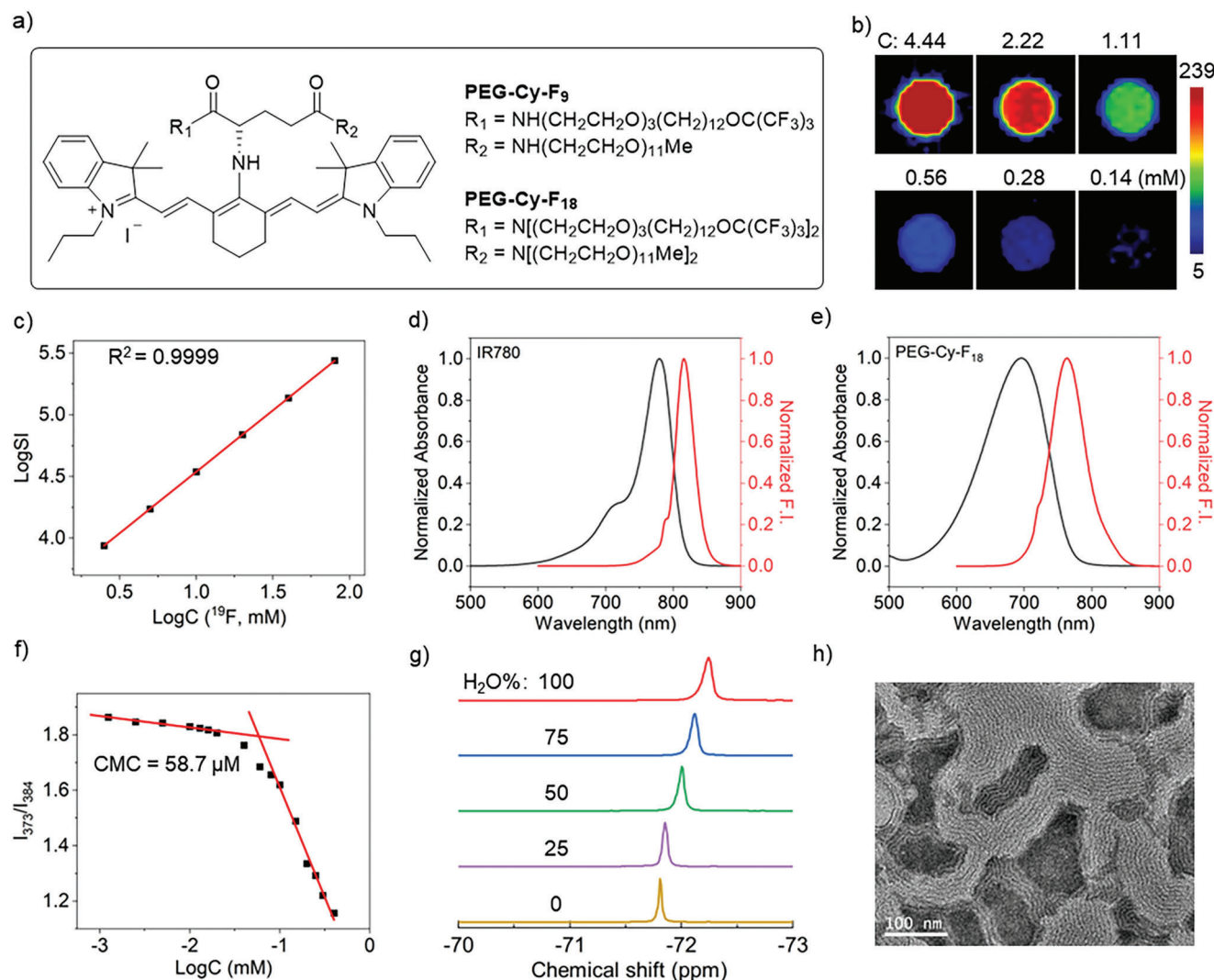


Figure 1. Structures of PEG-Cy-F₉ and PEG-Cy-F₁₈ a). ¹⁹F MRI phantom images (concentrations as indicated) b) and the logarithm plot of ¹⁹F signal intensity (SI) versus ¹⁹F concentrations ($R^2 = 0.9999$) c) of PEG-Cy-F₁₈. Normalized absorbance (black) and fluorescence emitting (red) spectra of IR780 d) and PEG-Cy-F₁₈ e). CMC measurement f), solvent-dependent ¹⁹F NMR spectra g), and TEM image h) of PEG-Cy-F₁₈. The corresponding Figure of linear PEG-Cy-F₉ can be found in Supporting Information.

to hypoxic tumors and promote PDT efficacy. In this manner, the as-prepared nanoparticles, denoted as SoFoTm/PEG-Cy-F₁₈, are expected to disassemble through the photothermal effect and generate reactive oxygens (ROS) through the photodynamic effect, facilitating controlled TAM release and effective chemo-PTT-PDT of breast cancer under NIR laser irradiation.

2. Results and Discussion

2.1. Synthesis and Characterization of PEG-Cy-Fs Amphiphiles

As designed, two types of fluorinated heptamethine amphiphiles were synthesized (Scheme S1, Supporting Information), including PEG-Cy-F₁₈ containing branched monodisperse PEG and fluorinated alkyl chains and PEG-Cy-F₉ containing linear ones (Figure 1a). The amphiphiles and their synthetic intermediates were fully characterized with ¹H/¹³C/¹⁹F NMR and mass

spectra (Supporting Information). A unified ¹⁹F NMR peak at -71.81 ppm was generated from the 18 or 9 symmetrical fluorine atoms in PEG-Cy-Fs, respectively (Figure S1a,b, Supporting Information), facilitating their sensitive ¹⁹F MRI detection. In the ¹⁹F MRI phantom experiments, PEG-Cy-Fs were imaged at a low ¹⁹F concentration of 5.0 mM, corresponding to 0.28 mM of PEG-Cy-F₁₈ and 0.56 mM of PEG-Cy-F₉, with a short data collection time of 256 seconds (Figure 1b, Figure S2a, Supporting Information). Furthermore, the logarithm of ¹⁹F signal intensity (SI) was proportional to the logarithm of the corresponding ¹⁹F concentration, which enables the accurate quantification of PEG-Cy-Fs concentration with ¹⁹F MRI SI (Figure 1c, Figure S2b, Supporting Information).

Next, the optical properties of PEG-Cy-Fs were studied. The replacement of the chlorine atom in IR780 with fluorinated amphiphilic building blocks caused a significant increase in fluorescence intensity and a dramatic blue shift of the maximum

Ultraviolet-Visible (UV-vis) absorbance from 780 nm (IR780) to 696 nm (PEG-Cy-F₁₈) and 694 nm (PEG-Cy-F₉), which may contribute to an intramolecular charge transfer between the donor and acceptor in PEG-Cy-Fs, as a chlorine atom has a stronger electron-withdrawing ability than a secondary amine group (Figure S3a,b, Supporting Information).^[14] When switching the solvent from methanol to water, considerable reductions in the maximum UV-vis absorbance were observed in PEG-Cy-Fs, indicating their high aggregation tendency in water. Compared to IR780, the PEG-Cy-Fs emitted considerably stronger and more blue-shifted NIR FL emission in methanol (Figure S3b, Supporting Information). Although they have far higher water solubilities than IR780, the FL emission of PEG-Cy-Fs was overwhelmingly quenched in water, probably due to the severe aggregation-caused quenching (ACQ). Notably, the Stokes shift of PEG-Cy-F₉ and PEG-Cy-F₁₈ reached 71 and 68 nm, respectively, which were significantly larger than that of IR780 (36 nm) (Figure 1d,e, Figure S3c, Supporting Information).

The observation of FL quenching in water promoted us to investigate the aggregation behavior of PEG-Cy-Fs. Using a UV-metric method, octanol-water partition coefficients (LogP) of PEG-Cy-Fs were measured as 1.05 and 1.72, respectively, indicating their relatively high hydrophobicity. Their aggregation behaviors were investigated with critical micelle concentration (CMC) measurements using a pyrene fluorescence probe method, which gave CMCs of 58.7 μM for PEG-Cy-F₁₈ and 77.8 μM for PEG-Cy-F₉ (Figure 1f, Figure S4c, Supporting Information), showing their high aggregation tendency. Additionally, a solvent-dependent ¹⁹F NMR study of PEG-Cy-Fs was carried out. When gradually switching the solvent from methanol to water, a 0.42 ppm up-field shift of the ¹⁹F peak was observed as a result of PEG-Cy-Fs aggregates formation in water, showing the transition of fluorocarbon moieties from a hydrophilic environment to a hydrophobic environment. Furthermore, the 5-fold broadening of the ¹⁹F NMR peak suggested that the mobility of fluorocarbon moiety was significantly restricted as a result of the aggregation in water (Figure 1g, Figure S5a, Supporting Information).^[15] The comparison of LogP, CMC, and ¹⁹F MRI detectable concentration of PEG-Cy-Fs indicated that their water solubility, ¹⁹F MRI sensitivity, lipophilicity, and aggregation tendency could be improved by duplicating the M-OEG and hydrofluorocarbon sidechains, providing a valuable strategy for manipulating their physicochemical properties.

Finally, the aggregates of PEG-Cy-Fs were analyzed using dynamic light scattering (DLS) and transmission electron microscope (TEM). Unfortunately, the aggregates were too polydispersed to be measured by DLS, which TEM images showed a “fingerprint-like” parallel fibers morphology (Figure 1h, Figure S5b, Supporting Information). The ACQ of FL and TEM images of PEG-Cy-Fs suggested that the heptamethine cyanine moieties may self-assemble in a “face-to-face” fashion and form the so-called nonfluorescent H-aggregates.^[16] Therefore, the peculiar molecular shape of PEG-Cy-Fs probably led to the dramatical blue shift in UV-vis absorption and FL emission, large Stokes shift, “fingerprint-like” aggregation, and ACQ of FL.

Table 1. The ingredients, particle size, and PDI of PEG-Cy-F₁₈ nanoparticles.

Entry	Ingredients	Size ^{b)}	PDI
1	PEG-Cy-F ₁₈ , S-oil (1:4) ^{c)}	— ^{d)}	— ^{d)}
2	PEG-Cy-F ₁₈ , S-oil (1:8, NP1)	185	0.15
3	PEG-Cy-F ₁₈ , S-oil (1:16, NP2)	203	0.22
4	PEG-Cy-F ₁₈ , S-oil (1:32, NP3)	250	0.21
5	PEG-Cy-F ₁₈ , S-oil, F-oil (1:7:4, NP4)	175	0.18
6	PEG-Cy-F ₁₈ , S-oil, F-oil (1:6:8, NP5)	177	0.17
7	PEG-Cy-F ₁₈ , S-oil, F-oil (1:4:16, NP6)	159	0.21
8	PEG-Cy-F ₁₈ , S-oil, F-oil (1:2:24, NP7)	160	0.21
9	PEG-Cy-F ₁₈ , S-oil, F-oil (1:0:32)	— ^{d)}	— ^{d)}
10	PEG-Cy-F ₁₈ , S-oil, F-oil, TAM (1:6:8:1.4, NP8)	162	0.16
11 ^{a)}	PEG-Cy-F ₁₈ , S-oil, F-oil, TAM (1:6:8:2.7, NP9)	179	0.14
12	PEG-Cy-F ₁₈ , S-oil, F-oil, TAM (1:6:8:5.4, NP10)	167	0.19
13	PEG-Cy-F ₁₈ , S-oil, F-oil, TAM (1:6:8:10.8, NP11)	191	0.18

^{a)} Ingredients in 10 mL PBS for **NP9**: 28 mg of PEG-Cy-F₁₈, 55 mg of soybean oil (S-oil), 50 mg of F-oil, and 10 mg of TAM; ^{b)} Size is the diameter in nm; ^{c)} Molar ratio of ingredients; ^{d)} No apparent spherical nanoparticles were detected by DLS.

2.2. Formulation and Characterization of SoFoTm/PEG-Cy-F₁₈

With a higher ¹⁹F MRI sensitivity and aggregation tendency, PEG-Cy-F₁₈ was utilized to construct theranostic nanoparticles. Notably, branched M-OEG sidechains have been reported to be more effective in PEGylating nanoparticles for higher stability, longer in vivo half-time, and lower immunogenicity purposes.^[17] Since PEG-Cy-F₁₈ was self-assembled into “fingerprint-like” parallel fibers, soybean oil (S-oil, Figure S1, Supporting Information) was then employed to promote the formation of monodisperse spherical nanoparticles by providing a hydrophobic core. Meanwhile, the soybean oil core was able to dissolve the hydrophobic moieties of PEG-Cy-F₁₈, break up the H-aggregation, and thus “turned on” the FL. After optimization of the PEG-Cy-F₁₈ to soybean oil molar ratio (Table 1, entries 1–4), monodispersed spherical nanoparticles **NP1** (So/PEG-Cy-F₁₈) with an appropriate particle size of 185 nm and a polydispersity index (PDI) of 0.15 were detected by DLS from a solution of 1:8 mixture (Figure 2a).

To improve the ¹⁹F MRI sensitivity, we employed 1,11-diperfluoro-tert-butoxyundecane (F-oil, Scheme S1, Supporting Information) with a similar structure to the sidechain of PEG-Cy-F₁₈ to partially replace the soybean oil in So/PEG-Cy-F₁₈, which may generate a unified intense ¹⁹F NMR peak without compromising stability and monodispersity of the nanoparticles. Notably, fluorocarbons are well-known for their high oxygen solubility and their nanoparticles have been approved by US FDA as blood substitutes, which may deliver oxygen to hypoxic tumors and enhance the efficacy of PDT. As expected, PEG-Cy-F₁₈ and F-oil gave very close singlet ¹⁹F NMR peaks at −73.59 and −73.61 ppm, respectively, while their mixture showed a pseudo singlet ¹⁹F NMR peak (Figure S1c, Supporting Information). A series of stable and monodispersed nanoparticles **NP4–NP7**

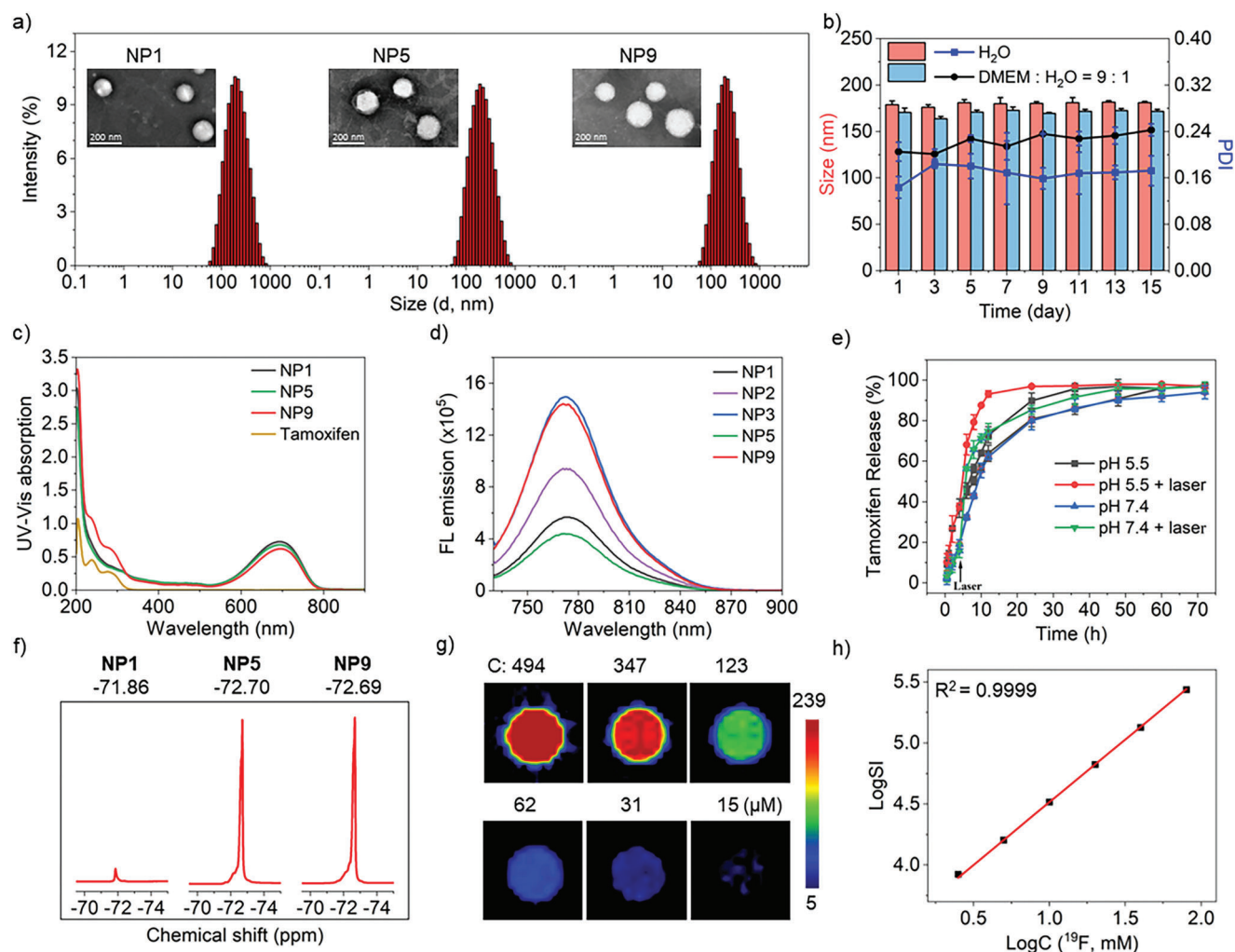


Figure 2. DLS and TEM of nanoparticles **NP1**, **NP5**, and **NP9**, scale bar: 200 nm a). Average particle size and PDI of three **NP9** samples in water and DMEM medium at 4 °C for 15 days. Data were presented as mean \pm SD ($n = 3$) b). UV-vis absorbance spectra of **NP1**, **NP5**, **NP9**, and TAM c). FL emission spectra of **NP1**, **NP2**, **NP3**, **NP5**, and **NP9** d). TAM release curves of **NP9** under the indicated conditions. Data were presented as mean \pm SD ($n = 3$) e). Partial ^{19}F NMR spectra of **NP1**, **NP5**, and **NP9** ($C_{\text{PEG-Cy-F}_{18}} = 1 \text{ mM}$) f). ^{19}F MRI phantom images of **NP9** at the indicated PEG-Cy-F₁₈ concentrations (g, $R^2 = 0.9999$) and the logarithm plot of ^{19}F signal intensity (SI) versus ^{19}F concentrations h). **NP1** (So/PEG-Cy-F₁₈), **NP5** (SoFo/PEG-Cy-F₁₈), **NP9** (SoFoTm/PEG-Cy-F₁₈).

were prepared by replacing 1 equivalent of S-oil in nanoparticles So/PEG-Cy-F₁₈ with 4 equivalent of F-oil (Table 1, entries 5–8). After evaluating the stability of the nanoparticles, **NP5** (SoFo/PEG-Cy-F₁₈) was identified as stable and monodispersed nanoparticles (Figure 2a). It was found that S-oil was necessary to generate monodisperse nanoparticles. When all S-oil in nanoparticles So/PEG-Cy-F₁₈ was replaced by F-oil, no apparent spherical nanoparticle was detected by DLS (Table 1, entry 9).

TAM, a hydrophobic breast cancer drug with a conjugated aromatic system (Scheme S1 in Supporting Information), was selected to realize the chemotherapy and promote the PDT efficacy of the nanoparticles via inhibiting mitochondrial complex I. Fortunately, a series of drug-loaded monodispersed nanoparticles **NP8–NP11** were obtained with high drug loadings of up to 23.1% after adding 1.3, 2.7, 5.4, and 10.8 equivalent TAM to the oil phase, respectively (Table 1, entries 10–13). Among the nanoparticles, **NP9** (SoFoTm/PEG-Cy-F₁₈) maintained highest monodis-

persity and stability at 4 °C in both water and cell culture medium DMEM (Figure 2b) for over 15 days. A high TAM encapsulation rate of 96% was determined for SoFoTm/PEG-Cy-F₁₈ using an HPLC method.

With the stable and monodispersed nanoparticles So/PEG-Cy-F₁₈, SoFo/PEG-Cy-F₁₈, and SoFoTm/PEG-Cy-F₁₈ in hand, their physicochemical properties were investigated. First, the nanoparticles exhibited a maximum UV-vis absorbance peak of around 695 nm (Figure 2c), which was the typical maximum UV-vis absorption of PEG-Cy-F₁₈. Notably, the typical UV-vis absorbance between 200 and 320 nm of TAM and SoFoTm/PEG-Cy-F₁₈ further confirmed the successful drug encapsulation. Second, compared to the ACQ FL of PEG-Cy-F₁₈, the FL emission of the nanoparticles was “turned on” with a maximum emission peak of $\approx 774 \text{ nm}$ (Figure 2d). When increasing the amount of S-oil from 8 equivalent (**NP1**) to 32 equivalent (**NP3**), the FL emission intensity of the corresponding nanoparticles increased by about

3-fold. In contrast, partially replacing S-oil with F-oil slightly reduced the FL emission in SoFo/PEG-Cy-F₁₈. Moreover, the encapsulation of TAM dramatically increased the FL emission intensity by about 3-fold in SoFoTm/PEG-Cy-F₁₈. These phenomenons indicated that the assembly of nanoparticles with an S-oil core and PEG-Cy-F₁₈ surface successfully broke up the H-aggregates of PEG-Cy-F₁₈ and “turned on” the FL emission, in which the dissolving of hydrophobic sidechains in S-oil reassembled the aggregation of PEG-Cy-F₁₈. Notably, TAM with hydrophilic 2-(dimethylamino)ethoxy head may also reassemble the nanoparticle surface and further “turn on” the FL emission. It should be pointed out that the quenched FL of PEG-Cy-F₁₈ and the high FL emission of its nanoparticles facilitate the selective FL monitoring of the intact nanoparticles without the interference of degraded ones.

In vitro drug release profile of TAM encapsulated in SoFoTm/PEG-Cy-F₁₈ was then studied in phosphate-buffered solutions (PBS) at pH 7.4 and 5.5, respectively. As shown in Figure 2e, 94% of TAM was released from SoFoTm/PEG-Cy-F₁₈ within 72 h at pH 7.4, while over 95% of TAM was released within 36 h at pH 5.5. After 4 h post the NIR laser exposure (750 nm, 5 min), a significantly accelerated drug release rate with over 93% of TAM release within 12 h at pH 5.5 was observed. These results demonstrated the pH/laser-prompted TAM release from SoFoTm/PEG-Cy-F₁₈, enabling controlled drug release and reducing nonspecific organ toxicity.

As expected, nanoparticles So/PEG-Cy-F₁₈, SoFo/PEG-Cy-F₁₈, and SoFoTm/PEG-Cy-F₁₈ gave a singlet ¹⁹F NMR peak of around -72.69 ppm, respectively (Figure 2f). Compared to So/PEG-Cy-F₁₈, the unified ¹⁹F NMR peak of PEG-Cy-F₁₈ and F-oil in SoFo/PEG-Cy-F₁₈ and SoFoTm/PEG-Cy-F₁₈ not only improved ¹⁹F signal intensity by 9-fold but also avoided ¹⁹F chemical shift imaging artifacts. Consequently, SoFoTm/PEG-Cy-F₁₈ were imaged at a low ¹⁹F concentration of 5.0 mM with a short data collection time of 256 s during the ¹⁹F MRI phantom experiments (Figure 2g), in which the logarithm of ¹⁹F SI was proportional to the logarithm of the corresponding ¹⁹F concentration (Figure 2h). Regarding PEG-Cy-F₁₈ concentration, the ¹⁹F MRI detectable concentration was decreased from 280 μM in PEG-Cy-F₁₈ solution to 31 μM in SoFoTm/PEG-Cy-F₁₈, a 9-fold improvement. Therefore, the formulation of PEG-Cy-F₁₈ with S-oil, F-oil, and TAM can deliver stable and monodisperse nanoparticles, which “turned on” FL emission and exhibited highly sensitive and quantitative ¹⁹F MRI.

2.3. Photothermal and Photodynamic Efficacy, Cytotoxicity, and Cell Uptake of SoFoTm/PEG-Cy-F₁₈

To assess the photothermal efficacy of the fluorinated nanoparticles, we used IR780 and PEG-Cy-Fs amphiphiles as controls and monitored temperature elevations with a thermal camera. After a 750 nm laser irradiation for 5 minutes at a power density of 1 W cm⁻², temperature elevations of about 15 °C, 21 °C, and 25 °C were observed from the 50 μM solutions of IR780, PEG-Cy-F₉, and PEG-Cy-F₁₈, respectively (Figure 3a). The photothermal conversion efficiency (PCE) was considerably improved after the modification of IR780 (PCE: 14.2%) to PEG-Cy-Fs amphiphiles (PCE: 22.0% for PEG-Cy-F₉, 25.9% for PEG-Cy-F₁₈).

However, after formulating PEG-Cy-F₁₈ into nanoparticles, the temperature elevations were reduced to less than 16 °C, in which the “turned-on” FL compromised the photothermal conversion. While SoFoTm/PEG-Cy-F₁₈ still exhibited a high PCE of 19.4%, which may elevate the temperature by 31 °C at a PEG-Cy-F₁₈ concentration of 75 μM (Red line in Figure 3a).

The photodynamic efficacy of the amphiphiles and their nanoparticles was then measured with a fluorescent probe, singlet oxygen sensor green (SOSG), to detect singlet oxygen (¹O₂).^[18] Compared with IR780, PEG-Cy-Fs amphiphiles produced significantly more ¹O₂ after a 750 nm laser irradiation at 1 W cm⁻², in which PEG-Cy-F₁₈ generated almost 2-fold more ¹O₂ than IR780 (Figure 3b). In contrast to the reduced photothermal efficacy after formulating with the oils, comparable photodynamic efficacies were found for So/PEG-Cy-F₁₈ and SoFo/PEG-Cy-F₁₈, while SoFoTm/PEG-Cy-F₁₈ produced much more ¹O₂ than PEG-Cy-F₁₈. Notably, 9-fold more ¹O₂ was generated when increasing the concentration of SoFoTm/PEG-Cy-F₁₈ from 0.5 μM to 4 μM (Figure S6a, Supporting Information). Furthermore, ¹O₂ generation capability of SoFoTm/PEG-Cy-F₁₈ was confirmed using electron spin resonance (Figure S6b, Supporting Information).

With the high photothermal and photodynamic capabilities, cytocompatibility and cytotoxicity of the nanoparticles were evaluated in normal human breast MCF-10A cells and human breast cancer MCF-7 cells, respectively. In MCF-10A cells, nanoparticles So/PEG-Cy-F₁₈ and SoFo/PEG-Cy-F₁₈ showed over 85% cell viability at a high PEG-Cy-F₁₈ concentration of 32 μM, indicating their good biocompatibility (Figure 3c). TAM-loaded SoFoTm/PEG-Cy-F₁₈ exhibited much better biocompatibility to MCF-10A cells than free TAM, benefiting from the slow TAM release profile under a neutral environment. Significant cytotoxicity to MCF-7 cells was found for the nanoparticles, especially for SoFoTm/PEG-Cy-F₁₈ (Figure 3d). The cytotoxicities were further improved after 750 nm laser irradiation at 0.4 W cm⁻² for 6 min, showing the PDT and PTT efficacy of the nanoparticles. Notably, because of its high TAM loading, SoFoTm/PEG-Cy-F₁₈ showed high cytotoxicity to MCF-7 cells even without a laser irradiation.

The cellular uptake and intracellular location of SoFoTm/PEG-Cy-F₁₈ in MCF-7 cells were then investigated by using confocal laser scanning microscopy. The confocal microscope images revealed the successful uptake of SoFoTm/PEG-Cy-F₁₈ by MCF-7 cells, which is crucial for optimal therapeutic response.^[19] During the 24-h incubation, the uptake of SoFoTm/PEG-Cy-F₁₈ in MCF-7 increased gradually (Figure 3e). Furthermore, the measurement of colocalized fluorescent signals (yellow) from SoFoTm/PEG-Cy-F₁₈ and mitochondrial tracking dye MitoTracker Green (MTG) revealed high mitochondria-targeting specificity (Figure 3f). The intrinsic mitochondria-targeting ability of IR780 and the electrostatic interaction between SoFoTm/PEG-Cy-F₁₈ (ζ-potential 36.7 ± 0.8 mV) and negatively charged mitochondrial membranes may account for the mitochondrial accumulation. Because of the quenched FL of PEG-Cy-F₁₈ and the high FL emission of its nanoparticles, the confocal images confirmed the delivery of intact SoFoTm/PEG-Cy-F₁₈ to mitochondrial. Given the inhibitory effects of TAM on mitochondrial respiratory rate by interacting with mitochondrial complex I,^[20] the delivery of TAM to mitochondrial through SoFoTm/PEG-Cy-F₁₈ is expected to achieve effective inhibition.

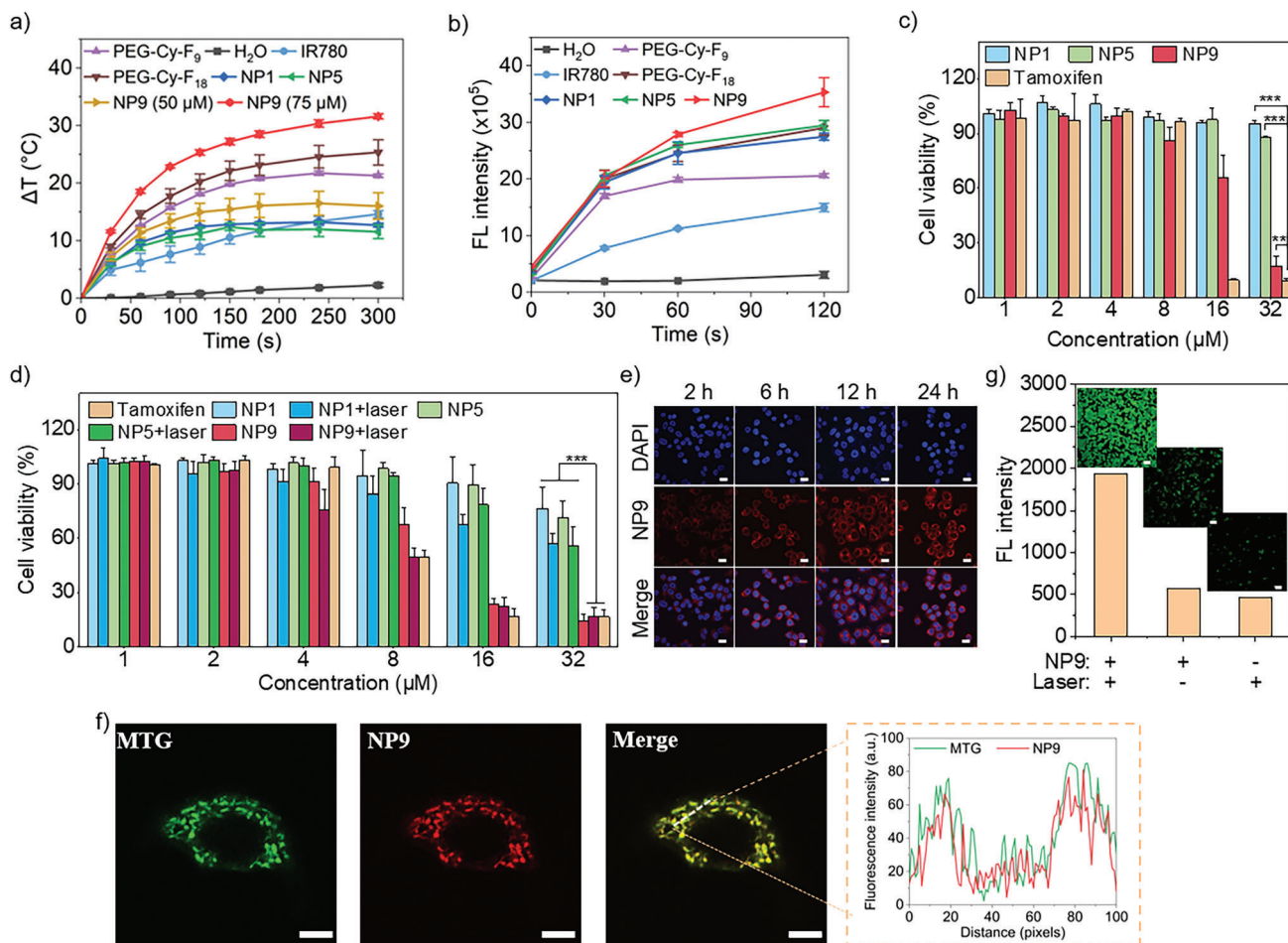


Figure 3. The plots of temperature elevation a) and SOSG FL intensity at 525 nm b) of IR780, PEG-Cy-Fs amphiphiles and their nanoparticles versus laser irradiation time. Biocompatibility assay toward MCF-10A cells c) and cytotoxicity assay toward MCF-7 cells d) of fluorinated nanoparticles with TAM as control using CCK-8 assay. The confocal microscope images of NP9-treated MCF-7 cells at the indicated time points after incubation, scale bar: 20 μm e) and colocalization with MTG in MCF-7 cells, scale bar: 10 μm f). DCFH-DA-stained MCF-7 cells treated with NP9 and PBS after laser irradiation, scale bar: 50 μm g). NP1 (So/PEG-Cy-F₁₈), NP5 (SoFo/PEG-Cy-F₁₈), NP9 (SoFoTm/PEG-Cy-F₁₈), MTG (MitoTracker Green). Data were presented as mean \pm SD ($n = 3$). p values are calculated using one-way ANOVA, ** $p < 0.01$, *** $p < 0.001$.

Meanwhile, benefiting from the slowed cellular O₂ consumption rate and favored ROS generation via TAM-inhibition of mitochondrial complex I, the hypoxia burden of tumors would be relieved, thereby synergistically improving the PDT efficacy of SoFoTm/PEG-Cy-F₁₈.^[21]

With fluorescence probe DCFH-DA, the generation of ROS in MCF-7 cells was studied, showing high green FL of DCFH-DA in cells treated with SoFoTm/PEG-Cy-F₁₈ (Figure 3g). Quantitative analysis indicated that, compared to PBS-treated cells and SoFoTm/PEG-Cy-F₁₈-treated cells, about 4-fold higher ROSS were generated in SoFoTm/PEG-Cy-F₁₈-treated cells after 750 nm laser irradiation at 0.4 W cm⁻² for 6 min.

2.4. In Vivo FLI, ¹⁹F MRI, and Photothermal Efficacy of SoFoTm/PEG-Cy-F₁₈

Taking the advantages of “turned-on” FL with large Stokes shift and high ¹⁹F MRI sensitivity, FLI, and ¹⁹F MRI were applied to

track the in vivo biodistribution of SoFoTm/PEG-Cy-F₁₈ in mice with xenograft MCF-7 tumors at different time points (Figure 4a). A strong FL of PEG-Cy-F₁₈ was observed in the tumor region 12 h after intravenous (i.v.) injection, which gradually increased and reached the peak 36 h post-injection (p.i.). The strong FL of PEG-Cy-F₁₈ in the tumor region was maintained for 10 days (Figure 4b), suggesting its high tumor retention and stable bioimaging ability. The remarkable tumor-targeted retention performance may be attributed to the proper particle size of SoFoTm/PEG-Cy-F₁₈ (179 nm), the “stealth effect” of branched PEG, and the tumor-targeted delivery potential of PEG-Cy-F₁₈ mediated by organic anion transporting polypeptides in tumor sites.^[22] The high accumulation of SoFoTm/PEG-Cy-F₁₈ in the tumor was further confirmed by the fluorescence images (Figure 4c) and intensity analysis (Figure 4d) of the internal organs and tumor collected 36 h p.i..

The in vivo photothermal effect of SoFoTm/PEG-Cy-F₁₈ was evaluated by monitoring temperature variation in the tumor region under laser irradiation. We established 36 h p.i. as the

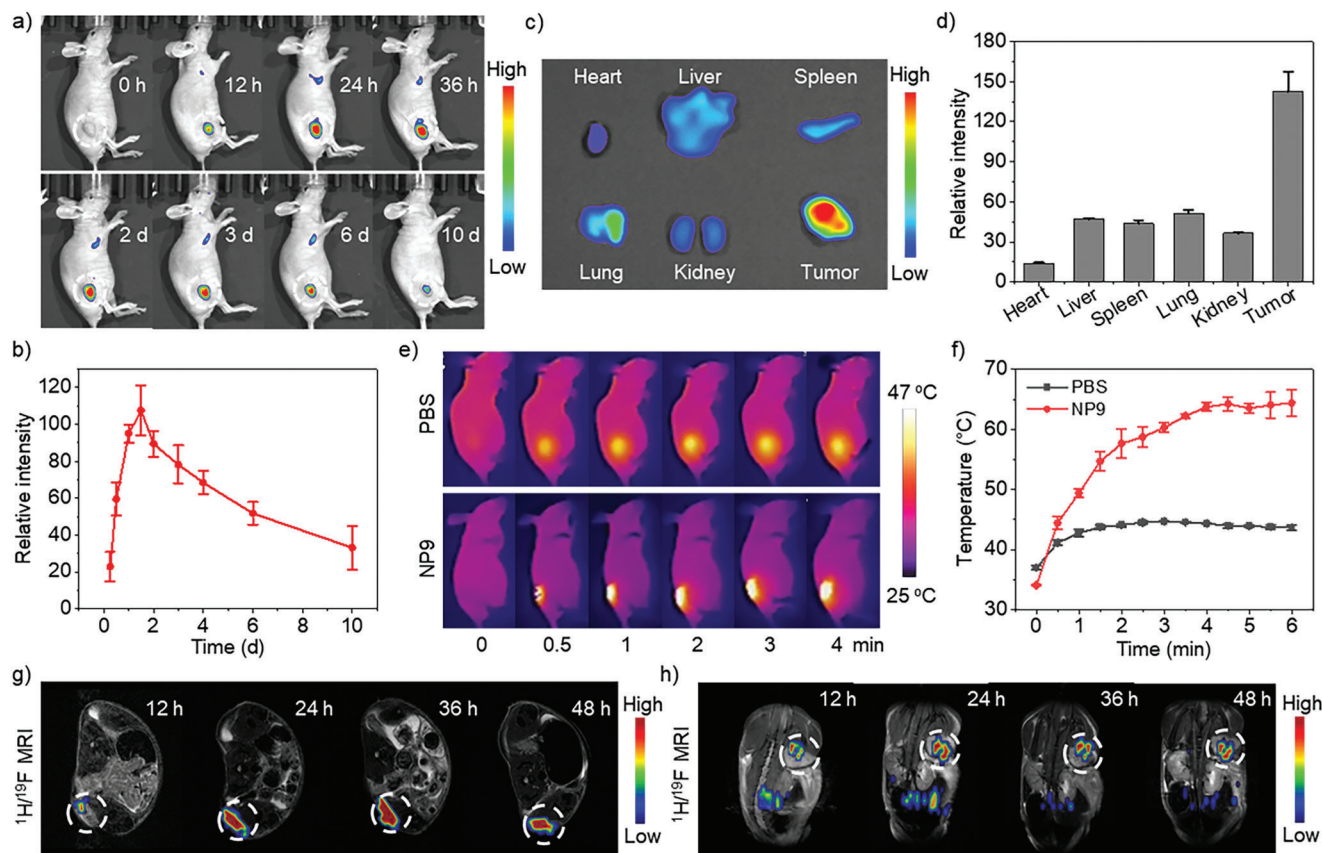


Figure 4. Whole-mice NIR FL images a), the plot of NIR FL intensities in tumor regions versus time b). NIR FL images c) and intensities d) of organs collected at the 36th-hour post-injection of SoFoTm/PEG-Cy-F₁₈. Photothermal images e) and the plot of tumor region temperature versus time f) under 750 nm laser irradiation at 1 W cm⁻² of mice 36 h after SoFoTm/PEG-Cy-F₁₈ and PBS injection. ¹⁹F MRI of mice after i.v. injection of SoFoTm/PEG-Cy-F₁₈ scanning in the transverse plane g) and coronal plane h). SoFoTm/PEG-Cy-F₁₈ was intravenously injected at 14 mg kg⁻¹ of PEG-Cy-F₁₈ to BALB/c nude mice with xenograft MCF-7 tumors. Data were presented as mean ± SD (*n* = 3).

optimum treatment time according to the time-dependent biodistribution of SoFoTm/PEG-Cy-F₁₈. After 4 min of 750 nm laser irradiation (1.0 W cm⁻²), the temperature of the tumor site rapidly increased to 63 °C. While the temperature increased to 41 °C under the same irradiation condition in the PBS-injected mice (Figure 4e). A thermal imaging camera recorded the treating process every 30 s, indicating that SoFoTm/PEG-Cy-F₁₈ could efficiently induce a temperature increase for PTT (Figure 4f). The excellent photothermal effect of SoFoTm/PEG-Cy-F₁₈ can not only facilitate effective PTT of cancer but also promote the selective in vivo TAM release in the tumor region.

Meanwhile, a time-dependent in vivo ¹⁹F MRI was conducted. Combined with the anatomic information offered by ¹H MRI, ¹⁹F MRI provided "hot-spot" images to visualize the in vivo biodistribution of SoFoTm/PEG-Cy-F₁₈ at the therapeutic dose (TAM concentration: 5 mg kg⁻¹). Consistent with the results obtained by FLI, the distribution of SoFoTm/PEG-Cy-F₁₈ was mainly observed in the tumor and reached the maximum accumulation in the tumor region at 36 h p.i. (Figure 4g,h). The tumor-target and retention properties would greatly benefit accurate tumor imaging and guide the subsequent therapy.

2.5. Chemo-PTT-PDT of Xenograft MCF-7 Breast Cancer with SoFoTm/PEG-Cy-F₁₈

Chem-PTT-PDT of xenograft MCF-7 human breast cancer with SoFoTm/PEG-Cy-F₁₈ was then carried out in BALB/c nude mice. When the tumor sizes reached ≈100 mm³, 5 groups of mice (*n* = 5) were i.v. injected with PBS (G1 and G2), TAM (G3), and SoFoTm/PEG-Cy-F₁₈ (G4 and G5) every 7 days, respectively. The treatment efficiency was assessed by measuring the tumor volume every two days after the treatment in each group. As presented in Figure 5a, the tumor growth rate is similar between the PBS group (G1) and the PBS+laser group (G2), suggesting that laser irradiation did not affect tumor growth. Compared to the PBS groups, a significant chemotherapy efficacy was observed in the TAM (G3) and SoFoTm/PEG-Cy-F₁₈ (G4) groups. SoFoTm/PEG-Cy-F₁₈ group exhibited higher tumor growth inhibition compared to the TAM group, probably due to the high tumor accumulation, mitochondria-targeting ability, and tumor retention properties. The therapeutic efficacy of SoFoTm/PEG-Cy-F₁₈ was further improved by 4 min of 750 nm laser irradiation (1 W cm⁻²) at 36 h p.i. (Figure 5a, G5). On the 21st day

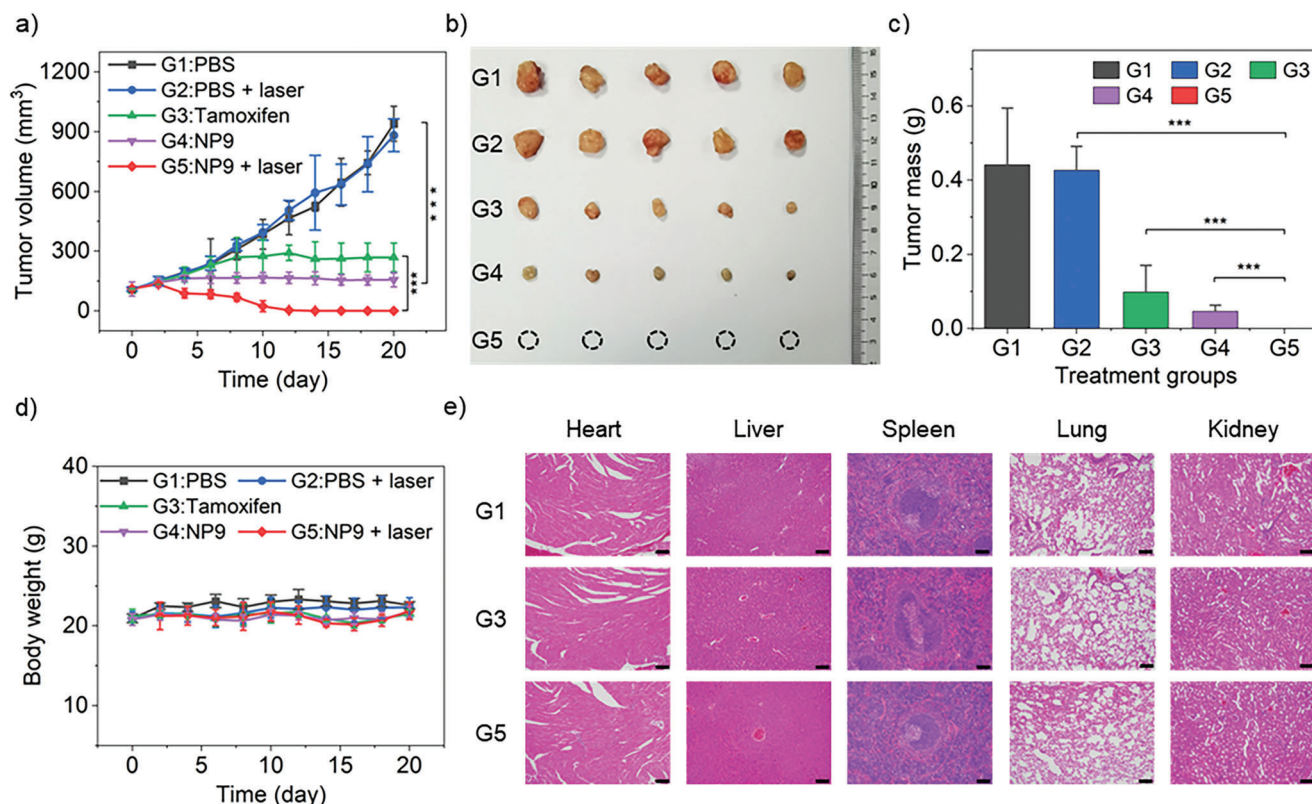


Figure 5. Tumor growth curves a), tumor photos b), tumor mass c), and body weight curves d) of five groups of mice treated with PBS (G1), PBS+laser (G2), TAM (G3), NP9 (G4), and NP9 +laser (G5). H&E staining of internal organs from G1, G3, and G5 (e, the rest groups can be found in Supporting Information). Data were presented as mean \pm standard deviation ($n = 5$, the asterisks indicate the statistical significance between G5 and G2, G3, *** $p < 0.001$). Irradiation of 750 nm laser at 1 W cm^{-2} for 4 min at tumor region 36 h after NP9 and PBS injection. Tumors and organs were collected on the 21st day. Scale bar: 100 μm . NP9 (SoFoTm/PEG-Cy-F₁₈). Data were presented as mean \pm SD ($n = 5$). P values are calculated using one-way ANOVA, *** $p < 0.001$.

of therapy, the mice were sacrificed and the tumors were collected (Figure 5b). Notably, complete tumor ablation was achieved in the five mice treated with SoFoTm/PEG-Cy-F₁₈ and laser irradiation. Both the tumor volume and tumor mass analysis showed significant therapeutic efficacy in G5 with $p < 0.001$ compared to PBS, TAM, and SoFoTm/PEG-Cy-F₁₈ groups, respectively (Figure 5a,c), demonstrating the effectiveness of the Chem-PTT-PDT combination therapy. No abnormal body weight changes were observed in all groups (Figure 5d). Furthermore, no noticeable tissue damage was observed from the H&E staining of internal organs collected after the treatment (Figure 5e, Figure S7, Supporting Information). These results suggested that highly efficient chem-PTT-PDT combination therapy of xenograft MCF-7 human breast cancer was achieved by SoFoTm/PEG-Cy-F₁₈ without apparent toxicity.

3. Conclusion

In summary, we have developed a monodisperse PEGylated and fluorinated heptamethine cyanine amphiphile PEG-Cy-F₁₈ with “all-in-one” theranostic functions to conveniently construct NIR light-responsive nanoparticles SoFoTm/PEG-Cy-F₁₈ for highly efficient dual-modal imaging-guided chemo-PDT-PTT of breast cancer. The delicate integration of photosensitizer, fluorescence

agent, ¹⁹F MRI agent, PEGylation agent, and surfactant into “all-in-one” amphiphile PEG-Cy-F₁₈ significantly simplifies the preparation of multifunctional theranostics with high convenience and precision, while avoiding the complexity, heterogeneity, and safety concerns of multiple functional entities. The larger Stokes shift (68 nm), proper LogP (1.05), improved photodynamic and photothermal efficiency, and ¹⁹F MRI capability rendered PEG-Cy-F₁₈ an excellent theranostic drug carrier. Through tuning the self-assembly of PEG-Cy-F₁₈, multifunctional theranostics SoFoTm/PEG-Cy-F₁₈ was conveniently prepared with high drug loading, “turned on” fluorescence, and 9-fold improved ¹⁹F MRI sensitivity, during which the rule of “like dissolves like” was employed to reassemble the “fingerprint-like” H-aggregates into stable monodisperse spherical nanoparticles and the rule was extended to “like emits like” to unify all the ¹⁹F signal in the nanoparticles into an ultrastrong one. Under the guidance of ¹⁹F MR-NIR FL dual-modal imaging, the treatment of SoFoTm/PEG-Cy-F₁₈ and NIR laser irradiation led to the complete ablation of the breast tumors, showing high therapeutic effectiveness of the multifunctional theranostics. These results demonstrated the great potential of “all-in-one” amphiphile PEG-Cy-Fs in the convenient, accurate, and standardized preparation of high-performance theranostics for imaging-guided drug delivery and cancer treatment, presenting a promising alternative to

complex ingredients in nanomedicine. It is noteworthy that the “all-in-one” amphiphiles PEG-Cy-Fs are also novel functionalized lipids, which could be employed as an “add-on” module to various nanoparticles, such as liposomes, nanoemulsions, polymerosomes, etc., and conveniently provide them with ^{19}F MR-NIR FL dual-modal imaging, photothermal therapy and photodynamic therapy, and PEGylation capabilities in an “on-call” manner.

4. Experimental Section

Preparation of Nanoparticles: Take the preparation of SoFoTm/PEG-Cy-F₁₈ as an example. 28 mg of PEG-Cy-F₁₈, 55 mg of soybean oil, 50 mg of F-oil, and 10 mg of TAM were dissolved in 1 mL of DCM, and 10 mL of deionized H₂O was added to the mixture. The dispersion was ultrasonicated at 400 W for 10 min, and the organic solvents were removed by rotary evaporation. SoFoTm/PEG-Cy-F₁₈ was obtained after filtering through a 450-nm PES membrane filter.

In Vitro ^{19}F MRI Experiments: ^{19}F MRI experiments were performed on a 400 MHz Bruker BioSpec MRI system. The temperature was maintained at 25 °C during the MRI experiment. The ^{19}F in vitro images were acquired using a spin-echo pulse sequence, method = RARE, matrix size = 32 × 32, SI = 20 mm, FOV = 3.0 cm, TR = 4000 ms, TE = 3.0 ms, scan time = 256 s.

Cytocompatibility and Cytotoxicity Assay: The cell cytotoxicity was evaluated using the CCK-8 kit. MCF-10A cells (1×10^4 cells per well) and MCF-7 cells (1×10^4 cells per well) were seeded in 96-well plates and incubated in 0.1 mL of DMEM containing 10% fetal bovine serum and 1% penicillin-streptomycin solution at 37 °C in a humidified 5% CO₂ atmosphere for 24 h. After removing the culture medium, 0.1 mL of the sample in fresh culture medium was added to each well and incubated for 24 h. Then, the medium was removed and the cells were washed with PBS (pH 7.4) three times, 0.1 mL of fresh medium was added. For the laser groups, the cells were illuminated using a 750 nm laser with an energy density of 0.4 W cm⁻² for 6 min. 0.1 mL of CCK-8 was added to each well. After incubation for 3 h, the optical density (OD) was measured at 450 nm using a microplate reader (BIORAD 550).

In Vitro Singlet Oxygen Detection: Singlet oxygen sensor green (SOSG) was employed to evaluate the singlet oxygen ($^1\text{O}_2$) generation. Take the detection of $^1\text{O}_2$ generated by SoFoTm/PEG-Cy-F₁₈ as an example. 0.5 mL of SOSG (4 μM) was added to SoFoTm/PEG-Cy-F₁₈ (0.5 mL, PEG-Cy-F₁₈ concentration: 4 μM), and the resulting solution was irradiated at 750 nm (1 W cm^{-2}) for 0, 20, 60, and 120 s, respectively. The fluorescence intensity was measured immediately at an excitation wavelength of 504 nm and an emission wavelength of 525 nm using a FluoroMax spectrofluorometer (HORIBA, Japan).

MitoTracker Green Assay: MCF-7 cells seeded on a Petri dish were cultured at 37 °C with 5% CO₂ for 24 h. Then, the cells were coincubated with SoFoTm/PEG-Cy-F₁₈ (PEG-Cy-F₁₈ concentration: 4 μM) at 37 °C in the dark for 6 h. The medium was removed, and the cells were washed with cold PBS (pH 7.4) three times and stained with MitoTracker Green (MTG) at 37 °C in the dark for 40 min. Cell images were acquired using confocal laser scanning microscopy (A1R/A1, Nikon).

Cellular ROS Detection: MCF-7 cells were coincubated with SoFoTm/PEG-Cy-F₁₈ (PEG-Cy-F₁₈ concentration: 4 μM) for 24 h.

The medium was removed and the cells were washed with PBS (pH 7.4) three times. 1 mL of DCFH-DA was added at a concentration of 10⁻⁵ M. After incubation for 30 min, the cells were irradiated by NIR laser irradiation (750 nm, 0.4 W cm⁻², 6 min), and the intracellular singlet oxygen generation was observed using confocal laser scanning microscopy (A1R/A1, Nikon).

Animals and Tumor Model: BALB/c female nude mice at 4–5 weeks old were purchased from Beijing Vital River Laboratory Animal Technology Co., Ltd. (Beijing, China). All animal experiments strictly followed the Guideline for Animal Care and Use, Innovation Academy for Precision Measurement Science and Technology, Chinese Academy of Sciences (APM23025T). The MCF-7 xenograft tumor model was established by subcutaneously injecting MCF-7 cells (1×10^7) suspended in 0.1 mL of PBS into the flank of the BALB/c nude mouse.

In Vivo FI Experiments: When the tumor volume reached about 200 mm³, the in vivo distribution and tumor accumulation in mice were studied at different time points after tail-vein injection of 0.1 mL of SoFoTm/PEG-Cy-F₁₈ (PEG-Cy-F₁₈ concentration: 14 mg kg⁻¹, TAM concentration: 5 mg kg⁻¹) by using an IVIS imaging system (PerkinElmer) (excitation/emission wavelength, 710/780 nm). The mice were sacrificed 36 h p.i., and the major organs and tumors were dissected for ex vivo NIR fluorescent imaging. The length (L) and width (W) of each tumor were measured, and the tumor volume (V) was calculated using the following formula: $V = L \times W^2 \times 0.5$.

In Vivo ^{19}F MRI Experiments: 0.1 mL of SoFoTm/PEG-Cy-F₁₈ (PEG-Cy-F₁₈ concentration: 14 mg kg⁻¹, ^{19}F concentration: 0.81 mmol kg⁻¹) was injected into the tail vein of MCF-7 tumor-bearing mice, and ^{19}F MRI was performed in vivo at different time points. $^1\text{H}/^{19}\text{F}$ magnetic resonance imaging experiments were performed on a 400 MHz Bruker BioSpec MRI system. ^1H MRI: method = RARE, TR = 2500 ms, TE = 33 ms, FOV = 3 × 3 cm, scan time = 160 s. ^{19}F MRI: method = RARE, TR = 3000 ms, TE = 3.0 ms, FOV = 3 × 3 cm, scan time = 32 min.

In Vivo Therapy: When the tumor volume reached ≈100 mm³, the mice bearing MCF-7 tumors were randomly divided into five groups (G1, G2, G3, G4, and G5), with five mice in each group. The mice in the G1 and G2 groups were intravenously injected with 0.1 mL of PBS, and the mice in the G3 group were intravenously injected with 0.1 mL of TAM solution (in 5% DMSO/40% PEG₄₀₀/55% 2-hydroxypropyl-β-cyclodextrin; TAM dose: 5 mg kg⁻¹), and the mice in the G4 and G5 groups were intravenously injected with 0.1 mL of SoFoTm/PEG-Cy-F₁₈ (TAM dose: 5 mg kg⁻¹). The mice in G2 and G5 were irradiated by a NIR laser (750 nm, 1.0 W cm⁻², 4 min) 36 h p.i., and the second laser treatment was performed on the 4th day after injection. The body weights and the tumor volumes were measured every 2 days. After 20 days of treatment, the mice were sacrificed, and the major organs and tumors were dissected to detect histological changes by H&E staining.

Statistical Analysis: The analyzed data are presented as mean ± standard deviation of $n \geq 3$ replicates. Statistical analysis was performed by one-way analysis of variance (ANOVA) followed by Tukey’s multiple comparisons using OriginPro 2023. Asterisks indicate significant differences: $p < 0.05$ was considered as the probability threshold for statistical significance, ** $p < 0.01$, *** $p < 0.001$.

Supporting Information

Supporting Information is available from the Wiley Online Library or from the author.

Acknowledgements

Y.L. and J.Z. contributed equally to this work. The authors thankful for financial support from the National Key R&D Program of China (2018YFA0704000), the National Natural Science Foundation of China (22077098, 21921004, 91859206, and 22004125), and the Knowledge Innovation Program of Wuhan-Basic Research (2022020801010137).

Conflict of Interest

The authors declare no conflict of interest.

Data Availability Statement

The data that support the findings of this study are available in the supplementary material of this article.

Keywords

¹⁹F MRI, fluorescence, heptamethine cyanine, phototherapy, self-assembly

Received: March 23, 2023

Revised: June 11, 2023

Published online: June 24, 2023

- [1] a) I. Dagogo-Jack, A. T. Shaw, *Nat. Rev. Clin. Oncol.* **2018**, *15*, 81; b) S. S. Kelkar, T. M. Reineke, *Bioconjugate Chem.* **2011**, *22*, 1879; c) A. Fernandez-Fernandez, R. Manchanda, A. J. McGoron, *Appl. Biochem. Biotechnol.* **2011**, *165*, 1628.
- [2] a) W. Fan, B. Yung, P. Huang, X. Chen, *Chem. Rev.* **2017**, *117*, 13566; b) J. Yao, F. Zheng, C. Yao, X. Xu, O. U. Akakuru, T. Chen, F. Yang, A. Wu, *WIREs Nanomed. Nanobiotechnol.* **2021**, *13*, e1682; c) A. C. Palmer, P. K. Sorger, *Cell* **2017**, *171*, 1678.
- [3] a) X. Li, J. F. Lovell, J. Yoon, X. Chen, *Nat. Rev. Clin. Oncol.* **2020**, *17*, 657; b) G. Feng, G.-Q. Zhang, D. Ding, *Chem. Soc. Rev.* **2020**, *49*, 8179; c) Q. Ma, X. Sun, W. Wang, D. Yang, C. Yang, Q. Shen, J. Shao, *Chin. Chem. Lett.* **2022**, *33*, 1681.
- [4] a) M. L. James, S. S. Gambhir, *Physiol Rev* **2012**, *92*, 897; b) D. E. Lee, H. Koo, I. C. Sun, J. H. Ryu, K. Kim, I. C. Kwon, *Chem. Soc. Rev.* **2012**, *41*, 2656.
- [5] a) L. Zhu, Y. Li, M. Jiang, C. Ke, H. Long, M. Qiu, L. Zhang, C. Ye, X. Zhou, Z.-X. Jiang, S. Chen, *ACS Appl. Mater. Interfaces* **2023**, *15*, 2665; b) S. Chen, L. Xiao, Y. Li, M. Qiu, Y. Yuan, R. Zhou, C. Li, L. Zhang, Z.-X. Jiang, M. Liu, X. Zhou, *Angew. Chem., Int. Ed.* **2022**, *61*, e202213495; c) A. M. Huynh, A. Müller, S. M. Kessler, S. Henrikus, C. Hoffmann, A. K. Kiemer, A. Bucker, G. Jung, *ChemMedChem* **2016**, *11*, 1568.
- [6] a) W. Bian, Y. Wang, Z. Pan, N. Chen, X. Li, W.-L. Wong, X. Liu, Y. He, K. Zhang, Y.-J. Lu, *ACS Appl. Nano Mater.* **2021**, *4*, 11353; b) M. Lan, S. Zhao, W. Liu, C.-S. Lee, W. Zhang, P. Wang, *Adv. Healthcare Mater.* **2019**, *8*, 1900132; c) N. Fernandes, C. F. Rodrigues, A. F. Moreira, I. J. Correia, *Biomater. Sci.* **2020**, *8*, 2990; d) S. Lee, S. Y. Kim, *ACS Appl. Nano Mater.* **2021**, *4*, 11849; e) I. Zmerli, N. Ibrahim, P. Cressey, S. Denis, A. Makky, *Mol. Pharmaceutics* **2021**, *18*, 3623.
- [7] a) K. K. Johnson, P. Koshy, J.-L. Yang, C. C. Sorrell, *Adv. Funct. Mater.* **2021**, *31*, 2104199; b) D. N. Heo, K. H. Min, G. H. Choi, I. K. Kwon, K. Park, S. C. Lee, in *Cancer Theranostics*, (Eds: X. Chen, S. Wong), Academic Press, Oxford **2014**, p. 457; c) S. Das, M. K. Das, in *Multi-functional Theranostic Nanomedicines in Cancer*, (Ed: M. K. Das), Academic Press, Cambridge **2021**, p. 307.
- [8] a) Q. Wang, Y. Dai, J. Xu, J. Cai, X. Niu, L. Zhang, R. Chen, Q. Shen, W. Huang, Q. Fan, *Adv. Funct. Mater.* **2019**, *29*, 1901480; b) S. He, C. Li, Q. Zhang, J. Ding, X.-J. Liang, X. Chen, H. Xiao, X. Chen, D. Zhou, Y. Huang, *ACS Nano* **2018**, *12*, 7272.
- [9] a) C. Zhang, L. Long, C. Shi, *Adv. Ther.* **2018**, *1*, 1800069; b) Y. Wang, T. Liu, E. Zhang, S. Luo, X. Tan, C. Shi, *Biomaterials* **2014**, *35*, 4116; c) E. Zhang, S. Luo, X. Tan, C. Shi, *Biomaterials* **2014**, *35*, 771; d) X. Zhao, H. Zhao, S. Wang, Z. Fan, Y. Ma, Y. Yin, W. Wang, R. Xi, M. Meng, *J. Am. Chem. Soc.* **2021**, *143*, 20828.
- [10] N. A. Daurio, S. W. Tuttle, A. J. Worth, E. Y. Song, J. M. Davis, N. W. Snyder, I. A. Blair, C. Koumenis, *Cancer Res.* **2016**, *76*, 3295.
- [11] S. Sharma, S.-F. Cheng, B. Bhattacharya, S. Chakkaravarthi, *Trends Food Sci. Technol.* **2019**, *91*, 305.
- [12] a) K. Chen, T. Wu, M. Jiang, A. Li, X. Peng, S. Chen, Z. Yang, X. Zhou, X. Zheng, Z.-X. Jiang, *Colloids Surf B Biointerfaces* **2022**, *215*, 112493; b) T. Tang, Q. Zhu, S. Liu, H. Dai, Y. Li, C. Tang, K. Chen, M. Jiang, L. Zhu, X. Zhou, S. Chen, Z. Zheng, Z.-X. Jiang, *Front Bioeng Biotechnol* **2022**, *10*.
- [13] a) A. M. A. Dias, M. Freire, J. A. P. Coutinho, I. M. Marrucho, *Fluid Phase Equilib.* **2004**, *325*, 222; b) E. P. Wesseler, R. Iltis, L. C. Clark, *J. Fluorine Chem.* **1977**, *9*, 137.
- [14] X. Peng, F. Song, E. Lu, Y. Wang, W. Zhou, J. Fan, Y. Gao, *J. Am. Chem. Soc.* **2005**, *127*, 4170.
- [15] M. B. Taraban, Y. Li, Y. Feng, E. V. Jouravleva, M. A. Anisimov, Z.-X. Jiang, Y. B. Yu, *RSC Adv.* **2014**, *4*, 54565.
- [16] Y. Deng, W. Yuan, Z. Jia, G. Liu, *J. Phys. Chem. B* **2014**, *118*, 14536.
- [17] a) M. Liu, J. Li, D. Zhao, N. Yan, H. Zhang, M. Liu, X. Tang, Y. Hu, J. Ding, N. Zhang, X. Liu, Y. Deng, Y. Song, X. Zhao, *Biomaterials* **2022**, *283*, 121415; b) M. Liu, D. Zhao, N. Yan, J. Li, H. Zhang, M. Liu, X. Tang, X. Liu, Y. Deng, Y. Song, X. Zhao, *Int. J. Pharm.* **2022**, *612*, 121365; c) Y. Li, X. Wang, Y. Chen, Z. Yang, Z.-X. Jiang, *Chem. Commun.* **2019**, *55*, 1895.
- [18] C. Flors, M. J. Fryer, J. Waring, B. Reeder, U. Bechtold, P. M. Mullineaux, S. Nonell, M. T. Wilson, N. R. Baker, *J. Exp. Bot.* **2006**, *57*, 1725.
- [19] Q. Yin, A. Pan, B. Chen, Z. Wang, M. Tang, Y. Yan, Y. Wang, H. Xia, W. Chen, H. Du, M. Chen, C. Fu, Y. Wang, X. Yuan, Z. Lu, Q. Zhang, Y. Wang, *Nat. Commun.* **2021**, *12*, 2385.
- [20] a) P. I. Moreira, J. Custódio, A. Moreno, C. R. Oliveira, M. S. Santos, *J. Biol. Chem.* **2006**, *281*, 10143; b) M. Li, Y. Shao, J. H. Kim, Z. Pu, X. Zhao, H. Huang, T. Xiong, Y. Kang, G. Li, K. Shao, J. Fan, J. W. Foley, J. S. Kim, X. Peng, *J. Am. Chem. Soc.* **2020**, *142*, 5380.
- [21] a) Y. L. Wan, L. H. Fu, C. Y. Li, J. Lin, P. Huang, *Adv Mater* **2021**, *33*, 2103978; b) L. Hong, J. M. Li, Y. L. Luo, T. Guo, C. S. Zhang, S. Ou, Y. H. Long, Z. Q. Hu, *Biomolecules* **2022**, *12*, 81.
- [22] C. Zhang, T. Liu, Y. Su, S. Luo, Y. Zhu, X. Tan, S. Fan, L. Zhang, Y. Zhou, T. Cheng, C. Shi, *Biomaterials* **2010**, *31*, 6612;